Flow Dynamics in the Aortic Arch and Its Effect on the Arterial Input Function in Cardiac Computed Tomography

Parastou Eslami[1]
Mechanical Engineering Department,
Johns Hopkins University,
Baltimore, MD 21218;
Department of Radiology,
Massachusetts General Hospital,
Harvard University,
Boston, MA 02114
e-mail: peslami1@mgh.harvard.edu

Jung-Hee Seo
Department of Mechanical Engineering,
Johns Hopkins University,
Baltimore, MD 21218

Albert C. Lardo
Department of Biomedical Engineering,
Johns Hopkins University,
Baltimore, MD 21218

Marcus Y. Chen
National Heart, Lung and Blood Institute (NHLBI),
National Institutes of Health,
Bethesda, MD 20892

Rajat Mittal
Department of Mechanical Engineering,
Johns Hopkins University,
Baltimore, MD 21218;
Division of Cardiology,
Department of Medicine,
Johns Hopkins University,
Baltimore, MD 21287

The arterial input function (AIF)—time-density curve (TDC) of contrast at the coronary ostia—plays a central role in contrast enhanced computed tomography angiography (CTA). This study employs computational modeling in a patient-specific aorta to investigate mixing and dispersion of contrast in the aortic arch (AA) and to compare the TDCs in the coronary ostium and the descending aorta. Here, we examine the validity of the use of TDC in the descending aorta as a surrogate for the AIF. Computational fluid dynamics (CFD) was used to study hemodynamics and contrast dispersion in a CTA-based patient model of the aorta. Variations in TDC between the aortic root, through the AA and at the descending aorta and the effect of flow patterns on contrast dispersion was studied via postprocessing of the results. Simulations showed complex unsteady patterns of contrast mixing and dispersion in the AA that are driven by the pulsatile flow. However, despite the relatively long intra-aortic distance between the coronary ostia and the descending aorta, the TDCs at these two locations were similar in terms of rise-time and up-slope, and the time lag between the two TDCs was 0.19 s. TDC in the descending aorta is an accurate analog of the AIF. Methods that use quantitative metrics such as rise-time and slope of the AIF to estimate coronary flowrate and myocardial ischemia can continue with the current practice of using the TDC at the descending aorta as a surrogate for the AIF. [DOI: 10.1115/1.4043076]

Keywords: arterial input function, contrast dispersion, computational fluid dynamics, aortic flow, cardiac computed tomography angiography

1 Introduction

Coronary computed tomography angiography (CTA) allows for noninvasive evaluation of coronary artery disease (CAD) and has proven to be a powerful tool for detection of this disease [1]. However, to be able to detect and quantify obstructive CAD accurately, image quality plays a major role. Besides poor signal to noise, low-contrast intensity contributes to poor image quality. This may be caused by improper image acquisition timing or slow contrast injection [2]. Therefore, to acquire good quality images with clear contrast enhancement in coronary lumen, it is crucial to optimize contrast injection and image acquisition timing. In coronary CTA imaging, this gate keeping is done by detecting the arrival of the contrast bolus at the coronary ostium to determine the optimal time for triggering the image acquisition [3,4]. The arterial input function (AIF) refers to the time–density curve (TDC) of the contrast concentration measured in Hounsfield units (HUs) at the coronary ostium.

In addition to optimizing image acquisition, AIF has been utilized in new methods for quantification of coronary blood flow [5–7]. For example, in transluminal attenuation flow encoding (TAFE) [6,7], the AIF up-slope at the coronary ostia is used to estimate coronary flow rates. However, it is quite difficult to directly acquire the TDC at the coronary ostia in coronary CTA and instead, the TDC at the descending aorta is used as a surrogate for the AIF. There are a number of factors that might generate differences in the two TDCs: (1) the two locations are separated along the aorta by a typical axial distance of about 20 cm and this would generate a finite time-lag between the TDCs at the two locations; (2) the flow in the ascending aorta is dominated by a complex transitional pulsatile jet [8,9] which is expected to affect the TDC at the coronary ostium; and (3) the significant curvature of the aortic arch and the three existing branches (left common carotid, left subclavian, and brachiocephalic artery) are expected to generate complex flow through the aortic arch [10]. These effects taken together could potentially generate significant differences between the TDC at the coronary ostia (i.e., the AIF) and in the descending aorta.

To our knowledge, no study to-date has examined or quantified the differences between the TDC at the aortic sinuses/coronary ostia and the descending aorta. The objective of this study is to use computational fluid dynamic (CFD) simulations in a patient-specific model of the aorta to investigate the validity of using the TDC at the descending aorta as a surrogate for the AIF at the coronary ostia. Here, we examine the effect of the complex hemodynamics through the aortic valve and aortic arch on the contrast dispersion and on the TDCs at these two locations.

2 Methods

2.1 Image Acquisition and Model Segmentation. The representative image series in this study was taken from a patient who had undergone a coronary artery bypass grafting procedure but had no aortic or aortic valve diseases. The image was acquired under an approved protocol with a retrospective ECG-gated acquisition protocol with the administration of 75 ml Iopamidol (Bracco

[1]Corresponding author.

Manuscript received June 13, 2018; final manuscript received February 8, 2019; published online xx xx, xxxx. Assoc. Editor: Keefe B. Manning.

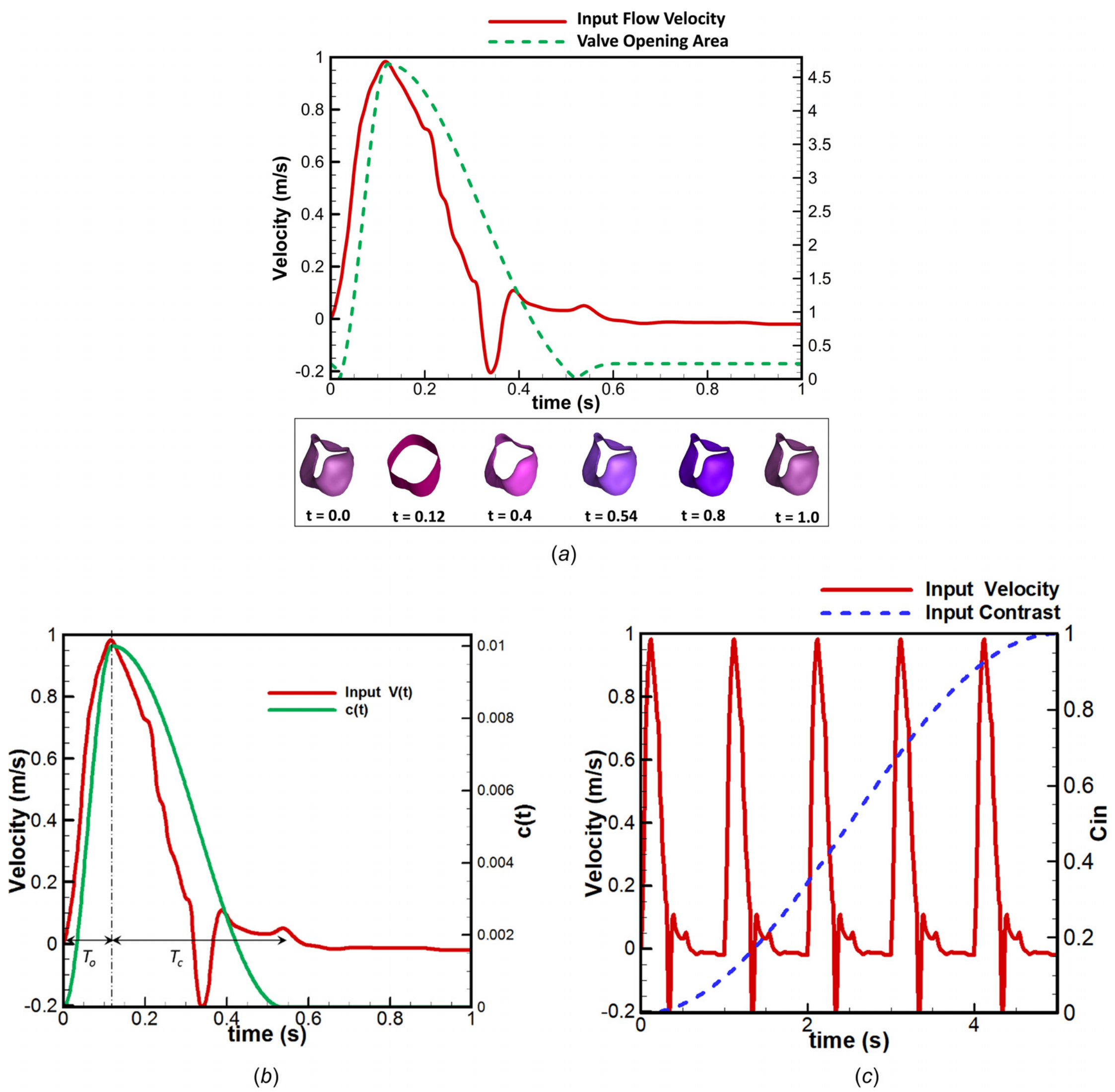

Fig. 1 (*a*) Time variation of flow velocity into the aorta and the valve opening area and the conformation of the valve leaflets during the cardiac cycle; (*b*) time variation of the valve compared with the velocity inflow profile: the opening time of the valve is defined as the time it takes to raise to the peak velocity and the closing phase is the time duration where the velocity drop beings in the inflow velocity until end systole; and (*c*) input contrast concentration for cardiac cycles compared with the velocity inflow profile

Diagnostics, Monroe Township, NJ) at a 5 cc/ml rate using a Toshiba 320 Aquilon One scanner (Toshiba Medical Systems Corporation, Otawara, Japan).

The 3D model of the aorta was segmented from the CTA dataset with a $0.351 \times 0.351 \times 0.5$ mm voxel resolution. Segmentation of aortic root as well as the ascending and proximal descending aorta (Fig. 2) was performed using a dynamic region-growing algorithm [11] at a thresholding level of 700 HU in Mimics (Mimics, Materialize Inc.). AQ6

2.2 Aortic Valve Modeling and Motion. It is essential to include a reasonably accurate model of the aortic valve in order to generate realistic flow patterns in the aorta [12–15]. However, none of the imaging modalities (Echo, CCTA or CMR) have either the spatial or the temporal resolution required to adequately resolve the motion of the valve leaflets. We, therefore, choose to employ a kinematic model of the aortic valve with a prescribed sinusoidal motion inspired by two previous numerical and experimental [16,17] and in vivo [18] studies. The valve velocity chosen in this study is a sinusoidal representation of what is reported in Bellhouse and Talbot [17]. In addition, the general motion of the valve prescribed in this study matches that of reported in Leyh et al. [18] with a faster opening and slower closure.

Based on the above studies, the velocity and displacement of the leaflets is prescribed as follows: AQ7

$$v_{\text{valve}}(x,t) = a(t) \cdot \mathbf{b}(\mathbf{x}) \qquad (1a)$$

$$d_{\text{valve}}(x,t) = c(t) \cdot \mathbf{b}(\mathbf{x}) \qquad (1b)$$

where $a(t)$ and $c(t)$ describe the time variation of valve velocity and displacement in time, respectively, and are defined in Eqs. 2(*a*) and 2(*b*) and $\mathbf{b}(\mathbf{x}) = \mathbf{x}_{\text{open}} - \mathbf{x}_{\text{close}}$ is the valve motion described in space.

$$a(t) = \begin{cases} \dfrac{\pi}{2T_o}\sin\left(\dfrac{\pi t}{T_o}\right), & t \le T_o \\[2ex] -\dfrac{\pi}{2T_c}\sin\left(\dfrac{\pi(t-T_o)}{T_c}\right), & T_o \le t \le T_c \end{cases} \qquad (2a)$$

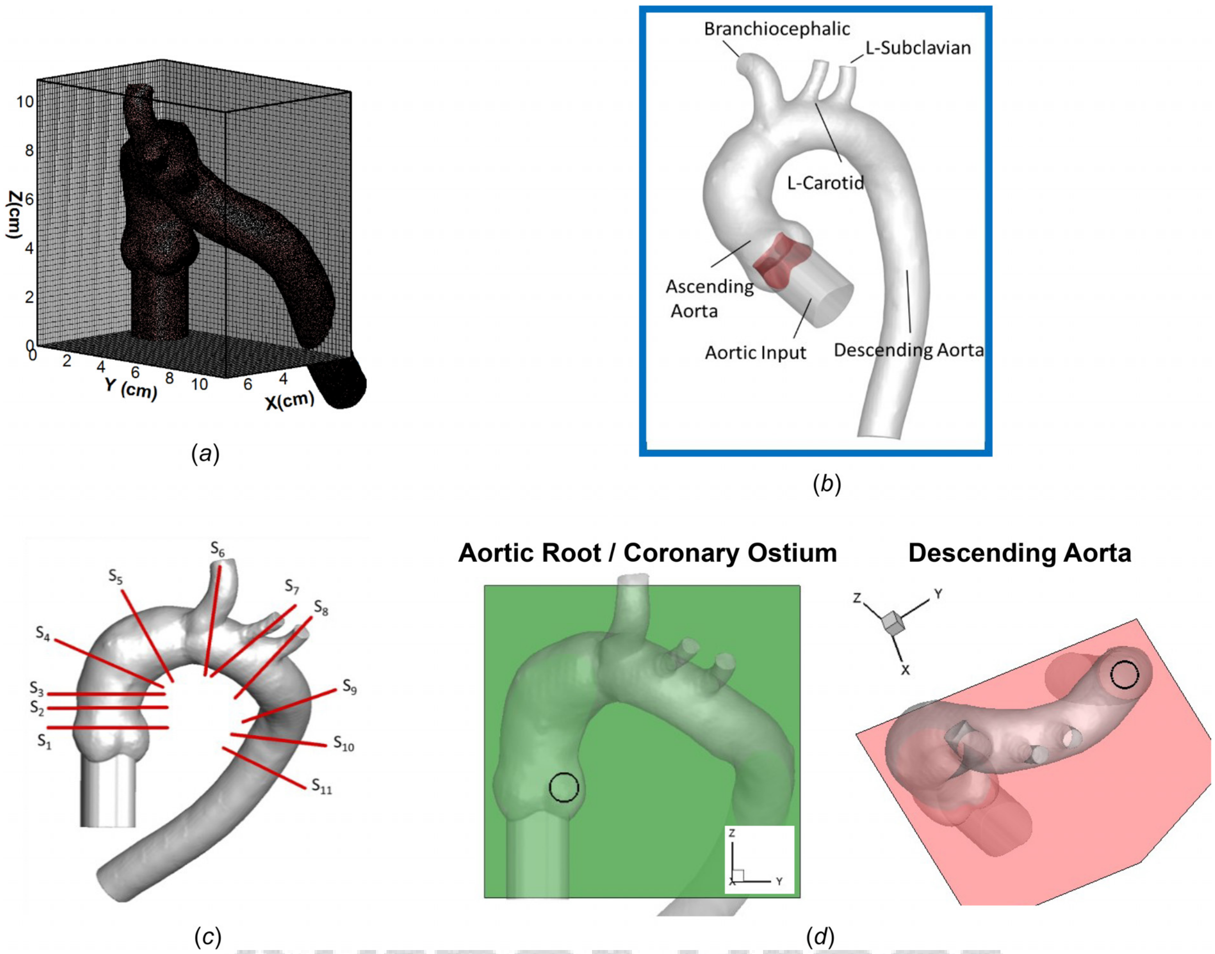

Fig. 2 (*a*) Immersed computational model where the gird is coarsened for visualization purposes, (*b*) the CFD ready model of aorta including the simple inflow tube along with the valve inserted at the aortic orifice shown at end diastole, (*c*) reference planes (S_1–S_{11}) used in the analysis of the simulation data, and (*d*) locations of ROIs used to determine the TDCs at the coronary ostium (left) and the descending aorta (right). The circles in all three planes are the true size ROI in which the contrast concentration was sampled.

$$c(t) = \int a(t)dt = \begin{cases} \frac{1}{2}\left(1-\cos\left(\frac{\pi t}{T_o}\right)\right), & t \le T_o \\ \frac{1}{2}\left(1+\cos\left(\frac{\pi(t-T_o)}{T_c}\right)\right), & T_o \le t \le T_c \end{cases} \tag{2b}$$

where T_o and T_c are opening and closing times of the valve, respectively, defined in Fig. 1(*b*). The resulting temporal variation of the valve orifice area as well as the input flow velocity for this study is shown in Fig. 1(*a*), where the opening time is chosen based on the rise-time to the peak velocity and the closing time is the remaining time from when velocity begins to drop to end of systole.

The valve model is a "semipatient-specific" model where the annulus of the aortic valve is extracted from the patient-specific geometry and the open and closed configurations are created as one continuous model based on the available literature [13,19]. In addition, since the open and closed forms of the valves do not have the same mesh topology, we perform a template-based surface registration using the large deformation diffeomorphic metric mapping method [20] (Fig. 1(*a*)).

2.3 Computational Fluid Dynamic Model and Governing Equations. Although blood is strictly a non-Newtonian fluid and exhibits shear-thinning behavior, in large vessels such as the aorta, where the shear rate is high, it can be treated as a Newtonian fluid. In this study, the blood flow is modeled by the Navier–Stokes equations for a Newtonian, viscous, and incompressible flow:

$$\frac{\partial u_j}{\partial x_j} = 0 \tag{3a}$$

$$\frac{\partial u_i}{\partial t} + \frac{\partial (u_i u_j)}{\partial x_j} = -\frac{1}{\rho}\frac{\partial p}{\partial x_i} + \nu \frac{\partial}{\partial x_j}\frac{\partial u_i}{\partial x_j} \tag{3b}$$

where $i, j = 1$, 2, and 3 are the coordinate directions, u_i are the flow velocity components, p is the static pressure of the fluid, ρ is the fluid density and ν is the fluid kinematic viscosity. The flow is solved via a previously implemented immersed boundary solver ViCar3D [21,22] that has been employed before in a number of hemodynamic modeling studies [23–26].

In ViCar3D, the contrast concentration is treated as a scalar dispersing through the flow and is modeled with an unsteady convection-diffusion equation as follows:

$$\frac{\partial C}{\partial t} + \frac{\partial}{\partial x_i}(u_i C) = \frac{\partial}{\partial x_j}\left(D\frac{\partial C}{\partial x_j}\right) \tag{4}$$

Table 1 List of flow and contrast concentration parameter

Opening time (T_o)	0.12 (s)
Closing time (T_c)	0.42 (s)
Peak velocity (V_{peak})	0.98 (m/s)
Stroke volume	118.24 (ml)
Heart rate	60 (beats/min)
Reynolds No. (Re)	2960
Schmidt No. (Sc)	1
Womersely No. (Wo)	14.39
Bolus duration time (T_d)	5 (s)
Bolus starting time (T_s)	0 (s)

where C is the contrast concentration and D is the coefficient of molecular diffusivity . The advection-diffusion is then solved implicitly in time using the Crank–Nicolson scheme for both the convective and diffusion term and a central-finite difference scheme is used is space resulting in second-order accuracy in both time and space.

Following previous studies [27,28], the inflow velocity profile (shown in Figs. 1(*a*) and 1(*b*) in red) is taken from the preclinical canine flow profile reported by Clark and Schultz [29]. However, the peak velocity (0.98 m/s) and the heart-rate has been adjusted to match the data reported in Gisvold and Brubakk [30] for humans. For the contrast concentration we also followed previous studies [6,7], and employed the following half cosine function to model the incoming contrast concentration

$$C_{\text{ositum}}(t) = C_{\min} + \frac{1}{2}(C_{\max} - C_{\min})\left(1 - \cos\left(\frac{\pi(t - T_s)}{T_d}\right)\right) \quad (5)$$

where $C_{\min}$ and $C_{\max}$ are the minimum and maximum concentration at the ostium, T_s is the arrival time of the bolus, and T_d is the time delay between the arrival time of bolus and the time the volumetric image is scanned. Figure 1(*c*) shows the fitting of a typical AIF curve obtained from a CT of a patient with the half-cosine model. In the current simulations we employ a rise-time for the bolus of five cycles, which is common for the CTA imaging procedure. At outflow boundaries (descending aorta, brachiocephalic, *L*-subclavian, and common carotid arteries in Fig. 2(*b*)), a convective boundary condition for both the velocity and the contrast is employed.

The kinematic viscosity of blood is chosen to be $\nu = 4\times10^{-6}\,\text{m}^2/\text{s}$; the mean flow velocity at the aortic orifice $U_{\text{mean}} = 20.57\,\text{cm/s}$ and the radius of the aortic inlet is $r = 1.5\,\text{cm}$. The heart-rate is chosen to be 60 bpm and therefore, the angular frequency is $= 1\,Hz$. The key nondimensional numbers that define the hemodynamics within the aortic arch are listed in Table 1. The average Reynolds number (Re) for the present model was approximately $\text{Re} = (2U_{mean}r/\nu) = 2960$, which is in line with the values reported in literature [31], while the Womersely number was $2r\sqrt{\omega/\nu} = 14.4$. Interestingly, the diffusivity (D) of the contrast agent in the blood is not well characterized and past studies have employed Schmidt numbers, $Sc = \nu/D$, ranging from 1 to 1000 [27,32]. In this study, we used $\text{Sc} = 1$ but have found than increasing this value by even three orders-of-magnitude does not have any noticeable effect on the results. Finally, the starting time and time delay for the contrast bolus are set to $T_s = 0$ (s) and $T_d = 5$ (s), respectively.

The aortic arch lumen used in this study is discretized with 223,990 triangular elements, while the aortic valve is discretized with 14,734 elements. The entire model surface is immersed in cuboidal domain of size $7.0\,\text{cm}\times11.0\,\text{cm}\times10.9\,\text{cm}$ with a $256\times256\times256$ (total of $\sim16.8\ \times10^6$ point) Cartesian grid (Fig. 2(*a*)). One cycle of the simulation required 7400 CPU hours on 256 processors on the Maryland Advanced Research Computing Center computer and we simulated a total of five cycles. This grid has been chosen after a grid refinement where we increased the grid size by a factor of two ($330\times330\times330$) and compared the results for the first two cycles against the data from the baseline grid. The key quantities of interest at slices S1–S11 (Fig. 2(*c*)) such as the mean flow rate and cross-sectional averaged contrast concentration were found to change by less than 5.0% and 4.4%, respectively. Given this, we considered the simulations on the baseline grid to be well converged. The time-step was 1×10^{-4} s which resulted in approximately 10,000 time steps per cardiac cycle and a Courant–Friedrichs–Lewy number of $\sim$0.32.

2.4 Time-of-Flight. The time-of-flight refers to the time it takes for the particle to travel from the ascending to descending aorta. The CFD calculations allow us to estimate the time-of-flight Γ for a particle of contrast to move from the aortic root to the descending aorta as follows $\Gamma_{1-11} = \sum_{i=1}^{10}(S_{i+1} - S_i)/((1-\alpha)U_{i+1} + \alpha U_i)$, where S_i is the axial distance of the ith plane along the aorta, U_i is the axial velocity on the corresponding plane that is used in this estimate of time-of-flight and α is defined as $\alpha = (|S_i|/|S_{i+1} - S_i|)$.

2.5 Time–Density Curves. The time–density curve in the descending aorta, $C_{\text{DA}}(t)$, is determined by establishing a circular ROI on the plane (Fig. 2(*d*)) which is nearly in the same lateral plane as the coronary ostium and estimating the average contrast concentration in this ROI. Similarly, the time–density curve at the coronary ostium $C_{\text{CO}}(t)$ (i.e., the AIF) is determined by defining a similar size ROI in the left coronary sinus of the aortic root. The following error function is used to quantify the difference between the two TDC profiles: $E(\tau) = (1/T_b)\int_0^{T_b}|C_{\text{CO}}(t) - C_{\text{DA}}(t-\tau)|dt$, where T_b is the time-to-peak of the bolus at the coronary ostium and τ is the time delay between the two TDCs. The time-lag between the two TDCs can be determined as the value of τ for which $E(\tau)$ attains its minimum.

3 Results

3.1 Flow Patterns. Figure 3 shows streamlines in the aortic arch at three different time points of early systole, peak systole when the valves open completely, and late systole. During early systole, the strong recirculation of flow at the valve tips (location indicated by arrows) is visible, but the rest of the flow streamlines in the aorta indicate a smooth laminar flow. Figure 3(*b*) shows the flow patterns at peak systole. The large-scale vortex structures induced by the curvature of the aortic arch are quite evident. Figure 3(*e*) shows the time-averaged axial flow velocity $\tilde{U}(S)$ at various cross-sectional planes. This plot shows that the velocity is highly nonuniform in each plane with narrow "streams" of high velocity.

3.2 Time–Density Curves. Figure 4 shows TDCs at the level of coronary ostium and the descending aorta sampled at a very fine time-interval of 0.01 s that is allowed by the CFD simulation. Current multidetector CT scanners such as the Aquilon-One typically monitor the bolus at sampling rates of 1–2 Hz. Figures 4(*c*) and 4(*d*) show the TDCs from the CFD simulation that has been down-sampled to time-intervals of 0.5 and 1 s. Figure 5(*a*) shows a plot of $E(\tau)$ for the TDCs at the coronary ostium, and the descending aorta and the minimum for this curve is located at $\tau = 0.19$ s. This indicates that the TDC at the descending aorta lags the TDC at the coronary ostium by 0.19 s (See Fig. 5(*a*)).

3.3 Time-of-Flight. Figure 5(*b*) shows a plot of $\tilde{U}(S)$ as well as $\tilde{U}^{\max}(S)$, the latter being the maximum time-averaged velocity on a given cross-sectional plane shown in Fig. 2(*c*). The transport time using both $\tilde{U}(S)$ and $\tilde{U}^{\max}(S)$ has been estimated and is found to be 0.55 s and 0.21 s, respectively.

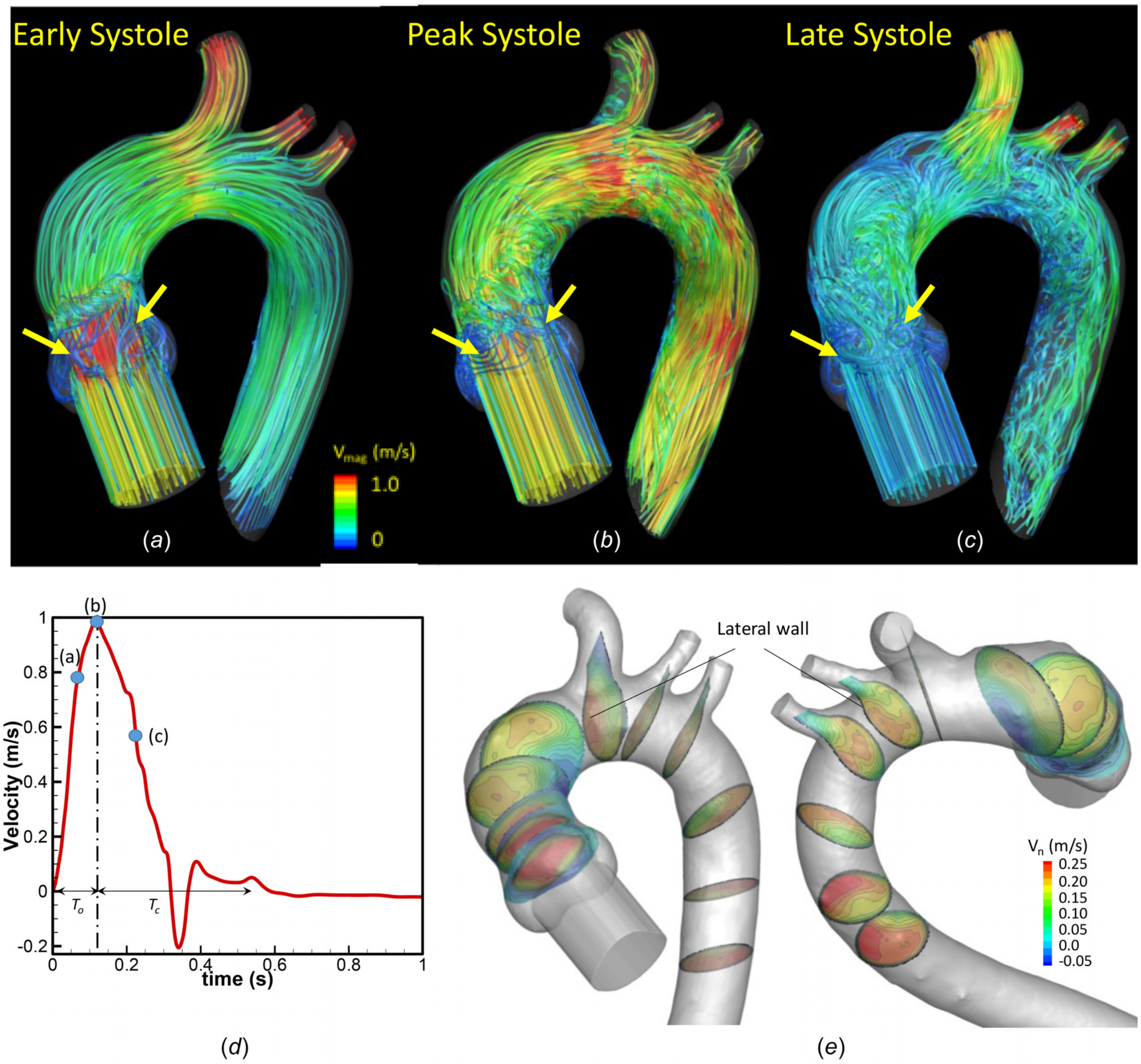

Fig. 3 Streamlines through the aortic arch colored by velocity magnitude at three different stages during with the arrows pointing toward the valve tips (*a*) early systole at $t = 1.06$ s, (*b*) mid systole at $t = 1.12$ s, and (*c*) late systole at $t = 1.33$ s. The stages are indicated in (*d*), and (*e*) two views of the contours of time-averaged axial velocity at selected cross sections.

4 Discussion

The flow pattern through the aortic arch calculated in this study is similar to that obtained in the computational study of Numata et al. [33]. The streamline patterns at late systole shown in Fig. 3(*c*) indicate a complex flow pattern in the entire ascending and descending aorta and this is driven by the destabilizing effect of the flow deceleration at this phase. The computed flow patterns in Fig. 3 can also be qualitatively compared favorably with the phase contrast MRI flow visualization in the aorta by in Markl et al. [8] and in Hope et al. [9]

The results from our simulations indicate that other than a small time-lag, the TDC's at the coronary ostium and descending aorta are very similar in shape and duration. The smaller than expected time-lag between the two TDCs is shown to be a consequence of the transport of contrast in the aortic arch by localized, high-velocity flow currents. This provides quantitative support for the current practice of using the TDC at the descending aorta as a surrogate for the AIF at the coronary ostium.

There is relatively minor qualitative difference between the TDCs at the coronary ostium and the descending aorta (Fig. 4(*b*)). These differences become even smaller when the TDCs are down-sampled at rates that are typical of cardiac CT protocols (Figs. 4(*c*) and 4(*d*)). The down-sampled TDC is also similar to what is observed clinically (Fig. 4(*a*)) where the effect of flow pulsatility in the aorta is much less apparent in TDC.

The small time-lag between the AIF at the coronary ostium and TDC in the descending aorta is rather surprising. This is given that the average velocity of the flow entering the aorta is about 18 cm/s (Fig. 1) and the approximate axial distance between the two planes where the TDCs are measured is about 16 cm. If the contrast is traveling at this average velocity, then the time-lag between the two TDCs should be about (16 cm)/(18 cm/s) = 0.88 s. This simple analysis, however, makes a number of assumptions including that the flow profile is uniform across the cross section, the cross-sectional area is constant along the aorta and that unsteady effects can be neglected. From the view point of cardiac CT, this observed behavior is intriguing and the current simulations enable us to explain this observation. The observation that the time-lag between the two TDCs of 0.19 s is very close to the time-of-flight of 0.21 s estimated from the time-averaged sectional maximum velocities and significantly smaller than the time-of-flight of 0.55 s estimated from the time and section-averaged velocities, is a clear indication that the localized streams of high

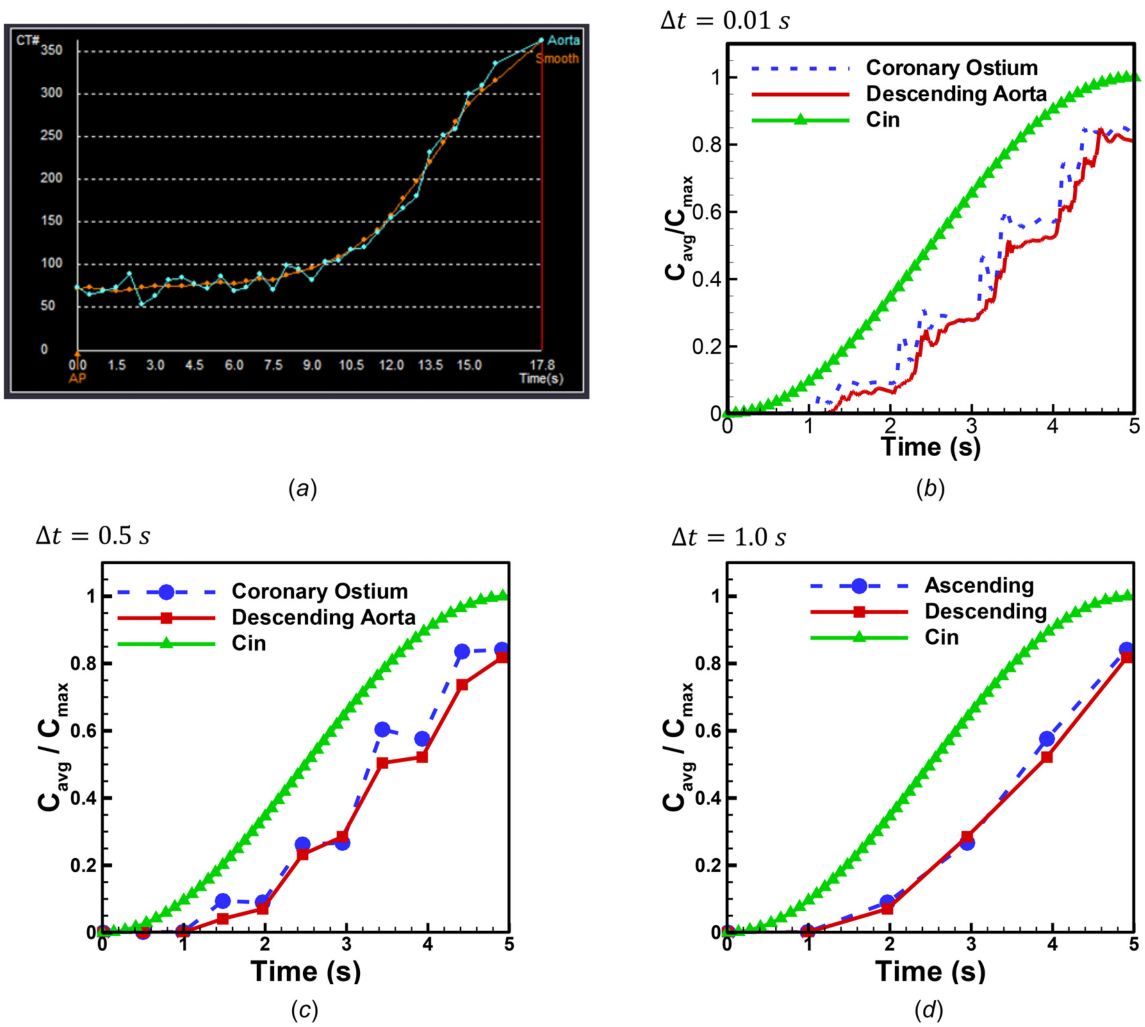

AQ15 **Fig. 4** (*a*) **A representative example of the TDC at the descending aorta measured during CTA that is used as a surrogate for the contrast bolus in the coronary ostium, (*b*) time profile of normalized cross-sectional averaged contrast concentration at the coronary ostium and the descending aorta at high temporal resolution of $\Delta t = 0.01\ s$. Sampled TDCs with lower temporal resolutions of, (*c*) $\Delta t = 0.5\ s$, and (*d*) $\Delta t = 1\ s$. The green line represents the inlet contrast concentration profile labeled as C_{in}. Note, there is no major difference in the two AIF's at ascending (dashed line) and descending (solid line) aorta.**

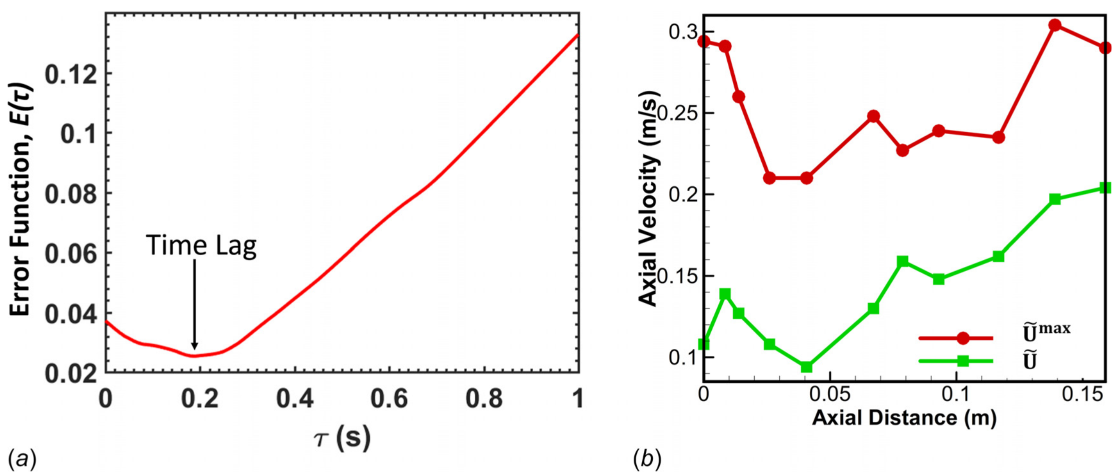

Fig. 5 (*a*) **Mean error between the two AIF curves at the coronary ostium and the descending aorta and (*b*) time-averaged axial velocity along the aorta; sectional mean velocity (green) and sectional maximum (red) on the 11 axial slices shown in Fig. 2(*b*)**

velocity flow that persist through the aortic arch, transport the contrast between the two locations much faster than would be suggested by the average velocity field.

The fact that the time-lag between the two TDCs is only 0.19 s, or 1/5th of the cardiac cycle, has important implications for methods that exploit AIF information. First, this time-lag is quite small, even negligible compared to the rise time of contrast in the coronary ostium, which ranges from about 5 to 10 s. Thus, any error in determining AIF rise time or upslope from the TDC at the descending aorta would be quite small. In fact, as has been shown earlier in this paper, the difference between these two TDCs is further masked by the relatively low sampling rate that is typical for bolus tracking in multidetector CT imaging. Interestingly, the time-lag between the two TDC is also smaller than the time-of-flight of flow through the major coronary vessels, which is on the order of 0.5 s [34]. For methods such as TAFE that combines upslope estimates with transluminal contrast gradients, this relatively small time-lag between the two TDCs also limits the errors associated with the use of the TDC at the descending aorta as a surrogate for the AIF.

A novelty of this work is that by obtaining the TDC's from the CFD, we overcome the technical limitations of CT imaging acquisitions such as locating the ROI and calculating the TDC's at any point in the ascending aorta, aortic arch and/or descending aorta. Our study indicates that the use of the TDC in the descending aorta as a surrogate for the AIF in methods such as TAFE may be reasonable. In addition, we have shown that the time-lag between the peaks of TDC is 0.19 s where information such as this could help improve the optimization of image acquisition. Beyond coronary CT angiography, the current results could find use in patients with aortic anomalies or conditions such as aortic dissection. Finally, a better understanding of TDCs in the aorta offered by this study could be utilized to improve calibration of contrast dosing protocols for patients.

Limitations: Although the simulation in the present proof-of-concept study incorporated many anatomical and physiological features of the aorta, some limitations remain. For example, blood was modeled as a non-Newtonian fluid and higher shear rate during systole, at the ascending aorta may have an effect on the hemodynamics. In this study, we used a simple prescribed valve motion and the fluid–solid interaction between the blood flow and valves are not modeled here. In addition, the aorta has been modeled as a stationary, nondeformable boundary and any effects of the dilation and movement of the aorta during the cardiac cycle on flow and contrast dispersion are ignored. This study focused on one inflow waveform, but we do expect that changes in peak flow rates and heart rate will affect the time-lag between the two TDCs. Given the highly nonlinear nature of flow development, it is difficult to speculate on these effects.

5 Conclusions

Hemodynamics and contrast dispersion in a physiologically realistic model of the aorta derived from CTA imaging has been investigated using CFD. The key conclusion of this study is that the TDCs at the coronary ostium (i.e., the AIF) and the descending aorta have very similar profiles and the time-lag between the two TDCs is a small fraction of the contrast rise time. This short time-lag is a result of the generation of spatially localized high-speed streams in the flow that accelerate the convection of contrast through the aortic arch. This study indicates that the use of the TDC at the descending aorta as a surrogate for the coronary AIF in computed tomography angiography is reasonable.

Funding Data

- Graduate Fellowship from the National Institutes of Health (Funder ID: 10.13039/100000002).

Author Disclosure

Under a licensing agreement between HeartMetrics, Inc. and the Johns Hopkins University, Drs. Mittal and Lardo are entitled to royalties on inventions that are related to work described in this manuscript. This arrangement has been reviewed and approved by the Johns Hopkins University in accordance with its conflict of interest policies. Drs. Mittal and Lardo are founders and equity holders in HeartMetrics, Inc.

Abbreviations

AA = aortic arch
AIF = arterial input function
CAD = coronary artery disease
CFD = computational fluid dynamics
CTA = computed tomography angiography
TAFE = transluminal attenuation flow encoding
TDC = time density curve

References

[1] Maurovich-Horvat, P., Ferencik, M., Voros, S., Merkely, B., and Hoffmann, U., 2014, "Comprehensive Plaque Assessment by Coronary CT Angiography," Nat. Rev. Cardiol., **11**(7), pp. 390–402.

[2] Abbara, S., Arbab-Zadeh, A., Callister, T. Q., Desai, M. Y., Mamuya, W., Thomson, L., and Weigold, W. G., 2009, "SCCT Guidelines for Performance of Coronary Computed Tomographic Angiography: A Report of the Society of Cardiovascular Computed Tomography Guidelines Committee," J. Cardiovasc. Comput. Tomogr., **3**(3), pp. 190–204.

[3] Meijboom, W. B., Meijs, M. F. L., Schuijf, J. D., Cramer, M. J., Mollet, N. R., van Mieghem, C. A. G., Nieman, K., van Werkhoven, J. M., Pundziute, G., Weustink, A. C., de Vos, A. M., Pugliese, F., Rensing, B., Jukema, J. W., Bax, J. J., Prokop, M., Doevendans, P. A., Hunink, M. G. M., Krestin, G. P., and de Feyter, P. J., 2008, "Diagnostic Accuracy of 64-Slice Computed Tomography Coronary Angiography. A Prospective, Multicenter, Multivendor Study," J. Am. Coll. Cardiol, **52**(25), pp. 2135–2144.

[4] Miller, J. M., Rochitte, C. E., Dewey, M., Arbab-Zadeh, A., Niinuma, H., Gottlieb, I., Paul, N., Clouse, M. E., Shapiro, E. P., Hoe, J., Lardo, A. C., Bush, D. E., de Roos, A., Cox, C., Brinker, J., and Lima, J. A. C., 2008, "Diagnostic Performance of Coronary Angiography by 64-Row CT," N. Engl. J. Med., **359**(22), pp. 2324–2336.

[5] George, A. C. A., Ichihara, R. T., Lima, T., and Lardo, J. A. C., 2010, "A Method for Reconstructing the Arterial Input Function During Helical CT: Implications for Myocardial Perfusion Distribution Imaging," Radiology, **255**(2), pp. 396–404.

[6] Lardo, A. C., et al., 2015, "Computed Tomography Transluminal Attenuation Flow Encoding (TAFE): Formulation, Preclinical Validation and Clinical Feasibility," JCCT, ■(■), ■. AQ9

[7] Eslami, P., Seo, J.-H., Rahsepar, A. A., George, R., Lardo, A. C., and Mittal, R., 2015, "Computational Study of Computed Tomography Contrast Gradients in Models of Stenosed Coronary Arteries," ASME J. Biomech. Eng., **137**(9), p. 091002.

[8] Markl, M., Draney, M. T., Miller, D. C., Levin, J. M., Williamson, E. E., Pelc, N. J., Liang, D. H., and Herfkens, R. J., 2005, "Time-Resolved Three-Dimensional Magnetic Resonance Velocity Mapping of Aortic Flow in Healthy Volunteers and Patients After Valve-Sparing Aortic Root Replacement," J. Thorac. Cardiovasc. Surg., **130**(2), pp. 456–463.

[9] Hope, M. D., Wrenn, S. J., and Dyverfeldt, P., 2013, "Clinical Applications of Aortic 4D Flow Imaging," Curr. Cardiovasc. Imaging Rep., **6**(2), pp. 128–139.

[10] Vasava, P., Dabagh, M., and Jalali, P., 2009, "Effect Aortic Arch Geometry Pulsatile Blood Flow: Flow Pattern Wall," ■, ■(1), pp. 1206–1209. AQ10

[11] Rangayyan, R., 2005, *Biomedical Image Analysis*, CRC Press-Taylor & Francis Group, ■. AQ12

[12] De Hart, J., Baaijens, F. P. T., Peters, G. W. M., and Schreurs, P. J. G., 2003, "A Computational Fluid-Structure Interaction Analysis of a Fiber-Reinforced Stentless Aortic Valve," J. Biomech., **36**(5), pp. 699–712.

[13] De Hart, J., Peters, G. W. M., Schreurs, P. J. G., and Baaijens, F. P. T., 2003, "A Three-Dimensional Computational Analysis of Fluid-Structure Interaction in the Aortic Valve," J. Biomech., **36**(1), pp. 103–112.

[14] Ranga, A., Bouchot, O., Mongrain, R., Ugolini, P., and Cartier, R., 2006, "Computational Simulations of the Aortic Valve Validated by Imaging Data: Evaluation of Valve-Sparing Techniques," Interact. Cardiovasc. Thorac. Surg., **5**(4), pp. 373–378.

[15] Makhijani, V., Yang, H., Dionne, P. J., and Thubrikat, M. J., 1997, "Three Dimensional Coupled Fluid Structure Simulations of Parcardial Bioprosthetic Aortic Valve Function," ASAIO, (43), pp. 387–392. AQ17

[16] Swanson, W. M., and Clark, R. E., 1973, "Aortic Valve Leaflet Motion During Systole. Numerical-Graphical Determination," Circ. Res., **32**(1), pp. 42–48.

[17] Bellhouse, B. J., and Talbot, L., 1969, "Fluid Mechanics of the Aortic Valve," J. Fluid Mech., **35**(4), pp. 721–735.

[18] Leyh, R. G., Schmidtke, C., Sievers, H. H., and Yacoub, M. H., 1999, "Opening and Closing Characteristics of the Aortic Valve After Different Types of Valve-Preserving Surgery," Circulation, **100**(21), pp. 2153–2160.

[19] El Faquir, N., et al., 2016, "Definition of the Aortic Valve Plane by Means of a Novel Dedicated Software Program: Proof of Concept and Validation With Multi Slice Computed Tomography," Int. J. Diagn. Imaging, **3**(1), pp. 63–71.

[20] Beg, M. F., Miller, M. I., Trouve, A., and Younes, L., 2005, "Computing Large Deformation Metric Mappings Via Geodesic Flows of Diffeomorphisms," Int. J. Comput. Vis., **61**(2), pp. 139–157.

[21] Seo, J. H., and Mittal, R., 2011, "A Sharp-Interface Immersed Boundary Method With Improved Mass Conservation and Reduced Spurious Pressure Oscillations," J. Comput. Phys., **230**(19), pp. 7347–7363.

[22] Mittal, R., Dong, H., Bozkurttas, M., Najjar, F. M., Vargas, A., and von Loebbecke, A., 2008, "A Versatile Sharp Interface Immersed Boundary Method for Incompressible Flows With Complex Boundaries," J. Comput. Phys., **227**(10), pp. 4825–4852.

[23] Seo, J. H., Abd, T., George, R. T., and Mittal, R., 2016, "A Coupled Chemo-Fluidic Computational Model for Thrombogenesis in Infarcted Left Ventricles," ■, ■(■), ■.

[24] Vedula, V., George, R., Younes, L., and Mittal, R., 2015, "Hemodynamics in the Left Atrium and Its Effect on Ventricular Flow Patterns," ASME J. Biomech. Eng., **137**(■), pp. 1–8.

[25] Vedula, V., Seo, J. H., Lardo, A. C., and Mittal, R., 2016, "Effect of Trabeculae and Papillary Muscles on the Hemodynamics of the Left Ventricle," Theor. Comput. Fluid Dyn., **30**(1–2), pp. 3–21.

[26] Zhu, C., Seo, J., Bakhshaee, H., and Mittal, R., 2018, "A Computational Method for Analyzing the Biomechanics of Arterial Bruits," ■, **139**(■), pp. 1–9.

[27] Kim, T., Cheer, A. Y., and Dwyer, H. A., 2004, "A Simulated Dye Method for Flow Visualization With a Computational Model for Blood Flow," J. Biomech., **37**(8), pp. 1125–1136.

[28] Shahcheraghi, N., Dwyer, H. A., Cheer, A. Y., Barakat, A. I., and Rutaganira, T., 2002, "Unsteady and Three-Dimensional Simulation of Blood Flow in the Human Aortic Arch," ASME J. Biomech. Eng., **124**(4), pp. 378–387.

[29] Clark, C., and Schultz, D. L., 1973, "Velocity Distribution in Aortic Flow," Cardiovasc. Res., **7**(5), pp. 601–613.

[30] Gisvold, S. E., and Brubakk, A. O., 1982, "Measurement of Instantaneous Blood-Flow Velocity in the Human Aorta Using Pulsed Doppler Ultrasound," Cardiovasc. Res., **16**(1), pp. 26–33.

[31] Ha, H., Ziegler, M., Welander, M., and Bjarnegård, N., 2018, "Age-Related Vascular Changes Affect Turbulence in Aortic Blood Flow," ■, **9**(■), pp. 1–10.

[32] Durant, J., Waechter, I., Hermans, R., Weese, J., and Aach, T., 2008, "Toward Quantitative Virtual Angiography: Evaluation With In Vitro Studies," International Symposium on Biomedical Imaging, Paris, France, May 14–17, pp. 632–635. AQ13

[33] Numata, S., et al., 2016, "Blood Flow Analysis of the Aortic Arch Using Computational Fluid Dynamics," Eur. J. Cardio-Thorac. Surg., **49**(■), p. ezv459. AQ14

[34] Poncelet, B. P., Weisskoff, R. M., Wedeen, V. J., Brady, T. J., and Kantor, H., 1993, "Time of Flight Quantification of Coronary Flow With Echo-Planar MRI," Magn. Reson. Med., **30**(4), pp. 447–457.